Atmospheric Research 236 (2020) 104811

Contents lists available at ScienceDirect

Atmospheric Research

journal homepage: www.elsevier.com/locate/atmosres

A multiscale analysis of the tornadoes of 30–31 May 2019 in south-central Chile

Bradford S. Barrett[a,*], Julio C. Marin[b,c], Martin Jacques-Coper[d,e]

[a] Oceanography Department, U.S. Naval Academy, USA
[b] Department of Meteorology, Universidad de Valparaíso, Chile
[c] Centro de Estudios Atmosféricos y Astroestadística, Universidad de Valparaíso, Chile
[d] Department of Geophysics, Universidad de Concepción, Chile
[e] Center for Climate and Resilience Research (CR)2, Chile

ARTICLE INFO

Keywords:
Tornadoes
Chile
Synoptic meteorology
Mesoscale modeling

ABSTRACT

On 30 and 31 May 2019, tornadoes occurred in the cities of Los Angeles and Talcahuano/Concepción in south-central Chile, in a region where tornado activity is not common. The main goal of this study was to analyze these tornadoes across multiple scales: synoptic, mesoscale, and subseasonal. On the synoptic scale, the tornadoes were associated with an anomalous 500-hPa trough and associated surface cyclone to the west of Chile. A strong (20+ m s^{-1}) low-level jet accompanied this trough, potentially enhanced by flow blocking by the Andes. A relatively warm and saturated surface layer combined with cold upper-level temperatures in the trough to yield 200–500 J kg^{-1} of CAPE on both days. This CAPE was accompanied by high levels of both deep-layer and low-level shear. Storm motions inferred by lightning swaths and GOES-IR imagery, along with estimates of storm motion and updraft helicity from a high-resolution WRF simulation, suggested this CAPE-shear combination was sufficient for the tornadic thunderstorms to be supercells. Finally, anomalies of sea level pressure, 500-hPa height, and surface dew point temperature from 27 to 31 May 2019 resembled long-term composite anomalies for MJO phases 1 and 2, suggesting a subseasonal link between the extreme event in Chile and convection in the tropics.

1. Introduction

The basic ingredients for deep, moist convection have been known for several decades: moisture, instability, and a source of lift (Doswell III et al., 1996). In the presence of vertical wind shear, the probability of a thunderstorm becoming severe increases (Weisman and Klemp, 1982), and many damaging tornadoes are often associated with severe storms in high-shear, high-buoyancy environments (Davies-Jones, 1986). Environments not characterized by high values of convective available potential energy (CAPE) or vertical wind shear receive less attention, but they can still support severe weather and tornadoes (Monteverdi and Quadros, 1994). Tornadic thunderstorms have been observed in so-called "high-shear, low-CAPE" environments in southern Australia (Hanstrum et al., 1998; Allen and Karoly, 2014), California (Hanstrum et al., 2002; Monteverdi et al., 2003), the U.S. southeast (Sherburn and Parker, 2014), and the British Isles (Mulder and Schultz, 2015), but there is currently no literature that suggests a threat of tornadoes from those conditions in Chile. Nevertheless, environments characterized by surface-based CAPE $\leq$500 J kg^{-1} and 0–6-km shear > 18 m s^{-1} were identified as one such "key subclass" of severe weather that merits attention because it tends to be overlooked by forecasters (Schneider et al., 2006), especially because tornadoes are possible within a broad spectrum of CAPE and shear combinations (Schneider and Dean, 2008).

The favorability of different combinations of CAPE and shear on severe weather was investigated globally by Brooks et al. (2003), and for the U.S. and Europe by Brooks et al. (2007) and Brooks (2009). Those studies generally note the ability of CAPE and 0–6-km bulk shear to collectively discriminate between severe and non-severe thunderstorm environments (Turcotte and Vigneux, 1987). Shear in the 0–1-km level and the surface lifting condensation level (LCL) were also identified as parameters that can discriminate storm severity. These and similar dynamic and thermodynamic parameters that favor tornadoes and severe thunderstorms were also identified by Rasmussen and Blanchard (1998), Rasmussen (2003), Craven and Brooks (2004), Romero et al. (2007), Mercer et al. (2009), Potvin et al. (2010), and

* Corresponding author at: Oceanography Department, U.S. Naval Academy, Annapolis MD 21402, USA.
E-mail address: bbarrett@usna.edu (B.S. Barrett).

https://doi.org/10.1016/j.atmosres.2019.104811
Received 14 August 2019; Received in revised form 2 December 2019; Accepted 19 December 2019
Available online 20 December 2019

Shafer et al. (2012). In general, higher values of CAPE, deep-layer (0–6 km) and low-level (0–1 km) shear, along with higher values of storm-relative helicity (SRH) and lower values of LCL height, all favor thunderstorms with the potential to produce tornadoes. Nevertheless, the primary emphasis in most tornado-parameter studies has been on supercells, particularly the supercell storm mode in the U.S. Great Plains, and there, the median value of CAPE tends to be high ($\geq$ 2000 J kg^{-1}). Other storm modes with typically lower values of CAPE, including quasi-linear convective systems, can also be associated with tornadoes (Trapp et al. 2005). As Brooks et al. (2003) note in their global climatology, oftentimes local factors - particularly topography - can modify the local conditions, thus creating environments favorable for low-level mesocyclones and tornadoes that might otherwise be missed. This is particularly important when tornadoes occur in regions heretofore thought to not be favored for tornadoes (Brooks et al., 2019), which is the case for south-central Chile (35–40°S). As argued by Hanstrum et al. (2002), there remains a need to increase our understanding of environments in which unusual tornadoes occur, and particularly so for regions with complex topography that tend to experience low-CAPE, high-shear conditions. Case studies such as this one serve to highlight the synoptic and mesoscale conditions under which those unusual tornadoes form, thus providing important context to forecasters looking to anticipate the next event.

Finally, there is an emerging body of literature that suggests convective weather events are sometimes connected to the evolution of the atmosphere on the subseasonal time scale (Thompson and Roundy 2013; Barrett and Gensini, 2013; Gensini and Marinaro, 2016; Baggett et al., 2018; Tippett, 2018; Gensini et al., 2019). Those studies have most often focused on the role of the Madden-Julian Oscillation (MJO; Madden and Julian, 1972) and Global Wind Oscillation (Weickmann and Berry, 2009) as drivers of tornado activity in the midlatitudes via the interaction of the extratropical circulation and Rossby waves emanating from tropical convection. Because some phases of the MJO have been shown to statistically favor different weather patterns in Chile (Barrett et al., 2012a; Barrett et al., 2012b; Ragsdale et al., 2013; Marin and Barrett, 2017; Rondanelli et al., 2019), it is important to examine this case of extreme weather in the subseasonal context. Information on subseasonal drivers of tornadoes could thus provide guidance concerning the predictability of future similar events.

The goals of this study are as follows: (1) we first examine the synoptic-scale conditions leading up to the tornado events in south-central Chile of 30 and 31 May 2019, with the aim to establish the synoptic patterns that were associated with the tornadoes; (2) we then use a numerical model to analyze the mesoscale severe-weather parameters present during each tornado, with the aim to compare the values of those parameters to values known to be favorable for tornadoes in other areas of the world; and (3) we finally explore the subseasonal state of the atmosphere in the weeks leading up to the tornadoes, with the aim to compare the conditions of May 2019 with the climatological base state observed during similar phases of one of the leading modes of subseasonal atmospheric variability, the MJO. The remainder of this article is organized as follows: the datasets, numerical simulation details, and methods used in the analysis are presented in section two; results of the synoptic, mesoscale, and subseasonal analyses of the two tornado events are presented in section three; and a summary and discussion are presented in section four.

2. Data and methods

2.1. Synoptic-scale environment

The synoptic-scale conditions leading up to the two tornado events were analyzed using the following data sets. First, 500-hPa geopotential heights and *u*- and *v*-wind components, 10-m wind *u*- and *v*-wind components, mean sea level pressure (MSLP), 2-m dew point, surface-based CAPE, and 850-hPa *u*- and *v*-wind components were taken from the Climate Forecast System Reanalysis version 2 (CFSRv2; Saha et al., 2011, available at https://rda.ucar.edu/datasets/ds094.0/) at 0.5° x 0.5° lat-lon grid spacing at 6-h intervals from 0000 UTC 25 May 2019 to 02 June 2019. Anomalies of each variable were calculated by subtracting the 1981–2010 long-term May–June mean (also available for download from the CFSRv2 website) from the value of each variable at each synoptic hour (00, 06, 12, and 18 UTC). Because 2-m dew point temperature tends to exhibit a diurnal cycle (with higher values in the day and lower at night), anomalies of 2-m dew point were calculated separately at each synoptic hour by subtracting the long-term mean for the corresponding synoptic hour. Furthermore, because the tornadoes analyzed in this study occurred right at the end of May, long-term monthly means for both May and June were averaged together, then used to calculate the anomalies. Equivalent potential temperature (θ_e) at two meters above ground level was calculated using the methodology of Davies-Jones (2008), who based their calculations mainly on the method of Bolton (1980). Second, daily values of sea surface temperature from 25 May to 02 June 2019 at 0.25° x 0.25° lat-lon grid spacing were taken from the NOAA OISSTv2 (Reynolds et al., 2007) dataset (available at https://www.esrl.noaa.gov/psd/data/gridded/data.noaa.oisst.v2.highres.html), and SST anomalies for each day were calculated by subtracting the long-term (1982–2010) mean for each Julian day from the daily observed SST. Infrared brightness temperatures from Channel 14 (11.2 μm wavelength) of the GOES-16 satellite at 2-km horizontal grid spacing (available at https://www.ncdc.noaa.gov/airs-web/search) were analyzed at 10-min intervals from 0000 UTC 30 May 2019 to 1200 UTC 01 June 2019. Lightning flashes detected by the GOES-16 Geostationary Lightning Mapper (GLM) (available at https://www.ncdc.noaa.gov/airs-web/search) and the World Wide Lightning Location Network (WWLLN, operated by the University of Washington and available at http://wwlln.net) were analyzed from 1200 UTC 30 May 2019 to 2359 UTC 31 May 2019. Finally, surface observations of 2-m temperature, 2-m dew point temperature, 10-m wind speed and direction, and MSLP were analyzed every 5 min from two surface observing stations: Los Angeles (37.45°S, 72.28°W) and Concepción (the Carriel Sur International Airport, 36.77°S, 73.06°W), both from 0000 UTC 28 May 2019 to 1600 UTC 01 June 2019 (available from https://climatologia.meteochile.gob.cl/).

2.2. WRF model simulation

Mesoscale conditions local to each tornado were analyzed using output from the Weather Research and Forecasting (WRF) Model (Skamarock and Coauthors, 2019) version 4.0. WRF is a three-dimensional non-hydrostatic regional numerical weather prediction model used for research and operational forecasting. The simulation was performed using three nested domains with horizontal resolutions of 9, 3, and 1 km (Fig. 1), 55 irregularly spaced vertical sigma levels, and a 50-hPa model top. The simulation was initialized at 0000 UTC 28 May 2019 and was run until 1200 UTC 01 June 2019. Initial and boundary conditions (every 6 h) were provided by the National Centers for Environmental Prediction (NCEP) Final (FNL) Analysis at 0.25° x 0.25°-degree horizontal grid spacing. An analysis nudging was applied to the coarsest domain (9 km horizontal resolution) to prevent the regional simulation from departing too much from the large-scale atmosphere provided by the FNL. Outputs from domains 2 and 3 were saved every 5 min. Because the CAPE, shear, and reflectivity from domains 2 and 3 were all very similar, output from the larger domain (domain 2) will be used for spatial and cross-section plots, and output from the inner domain (domain 3) will be used for point values.

The following physical parameterizations were used in the WRF simulation: the T microphysics scheme (Thompson et al., 2008), the four-layer Noah-MP land surface model (Niu et al., 2011), the Rapid Radiative Transfer Model (RRTMG, Iacono et al., 2008) parameterization for shortwave and longwave radiation, and the Mellor-Yamada Nakanishi Niino (MYNN, Nakanishi and Niino, 2006) Level 2.5

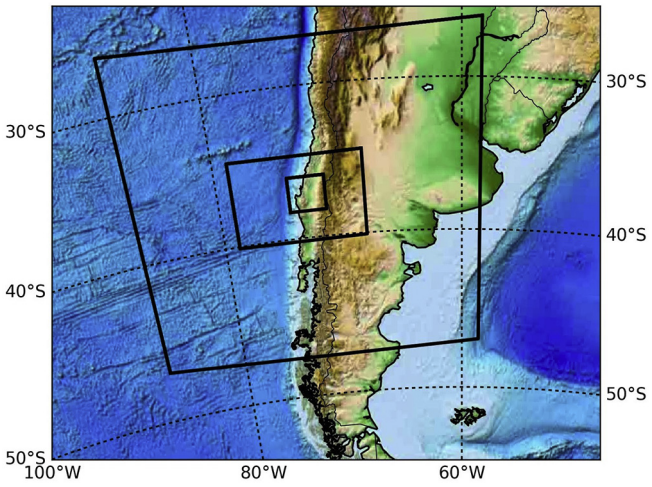

Fig. 1. Three nested WRF domain configuration used in the study with 9, 3, and 1 km horizontal resolutions.

parameterization for the planetary boundary layer. Additionally, the Betts-Miller-Janjic (Janjic, 1994) cumulus parameterization was used for the coarser domain (9 km), and no cumulus parameterization was applied to the two nested grids.

2.3. Subseasonal conditions

The subseasonal context of the two tornadoes was evaluated by comparing the conditions observed at the surface (MSLP and 2-m dew point temperature) and middle troposphere (500-hPa height) during late May 2019 with the average conditions seen in composite analyses based on the phases of the MJO. For this analysis, the NCEP-NCAR Reanalysis (Kalnay et al., 1996) was used to calculate synoptic-to-intraseasonal anomalies for the period May–June 1981–2019, and 2-m dew point temperature was calculated from the NCEP-NCAR Reanalysis following the approximation of Lawrence (2005). Anomalies of each variable were calculated by subtracting from the absolute values the 1981–2010 annual cycle and the respective seasonal anomaly for each year (e.g. for 2019, the 2019 May–June departure from the 1981–2010 May–June mean), following the methodology of Jacques-Coper et al. (2015). The phase and amplitude of the MJO was determined using the daily Wheeler and Hendon (2004)) Real-time Multivariate MJO (RMM) index (available http://www.bom.gov.au/climate/mjo/graphics/rmm.74toRealtime.txt). The RMM index is a time series of the first two leading principal components (RMM1 and RMM2) derived from empirical orthogonal functions of equatorially averaged (15°S–15°N) 850-hPa zonal wind, 200-hPa zonal wind, and outgoing longwave radiation. The RMM index is divided into eight phases, with each phase corresponding broadly to the geographic location of the MJO enhanced convective signal. For this study, an active MJO was considered as one with an amplitude $(RMM1^2 + RMM2^2)^{0.5} > 1.0$.

3. Results

3.1. Event evolution on the synoptic scale

On 30 May 2019 from approximately 2157–2205 UTC (1757–1805 local time), a tornado moved through the northeastern part of the city of Los Angeles, Chile (population approximately 130,000, altitude 140 m above sea level, 37.45°S, 72.33°W). The tornado was observed by multiple residents, several of whom filmed portions of it and shared those videos on social media platforms. A formal analysis by the Chilean National Weather Service (DMC, following its acronym in Spanish) (Vicencio et al., 2019), based on damage surveys conducted in the three weeks following the tornado, estimated that the tornado lasted 8 min and had a curved path of around 5 km moving primarily from north-northwest to south-southeast. The DMC's damage survey concluded the tornado in Los Angeles had a maximum intensity of EF-2 (wind speeds 178–217 km hr^{-1}). On the very next day, 31 May 2019, from approximately 1800–1815 UTC (1400–1415 local time), another tornado moved through the twin cities of Talcahuano and Concepción, Chile (Chile's second-largest city with a combined population approximately 1.3 million; altitude 10–30 m above sea level; 36.82°S, 73.05°W). Similar to the tornado of the day before, multiple residents filmed the tornado, and several of those videos appeared shortly thereafter on social media platforms. The formal analysis by the DMC (Vicencio et al., 2019) determined this tornado lasted 15 min and had a curved path of around 18 km, also primarily moving from northwest to southeast. The DMC's damage survey concluded the tornado in Talcahuano/Concepción had a maximum intensity of EF-1 (wind speeds between 138 and 177 km hr^{-1}).

The two tornadoes in south-central Chile occurred approximately 100 km apart, on consecutive days in a region with not only very few historical tornado records but also little expectations of such extreme phenomena (Brooks et al., 2003). As such, it is important to consider the synoptic-scale conditions leading up to the tornado events, particularly as such awareness can aid forecasters in advance of any future tornado events. At 1200 UTC on 28 May 2019, two troughs at 500 hPa were observed, one with an axis near 95°W and a deeper one near 130°W (Fig. 2a). Lower-tropospheric circulation at 850 hPa was cyclonic to the east of each of these two troughs, with wind speeds approaching 20 m s^{-1} (Fig. 2b). Two regions of anomalous low sea-level pressure were centered near 35°S 95°W (anomaly of −10 hPa) and 47°S 125°W (anomaly of −25 hPa) (Fig. 2c). As a result of the low-level cyclonic wind field, two regions of higher surface dew point temperature (10–15 °C) (Fig. 2d) and positive θ_e advection (Fig. 2e) extended from the subtropics (near 20°S) into the mid-latitudes (near 40°S). Finally, the 15 °C SST isotherm extended roughly along 40°S on 28 May 2019, with positive SST anomalies up to 2 °C extending from 110°W to 80°W, approximately ten latitude degrees either side of 40°S (Fig. 2f). These synoptic-scale conditions (an eastward-moving trough at 500 hPa, a mid-latitude surface cyclone, southward surface and lower-tropospheric flow to the east of a region of surface low pressure, positive θ_e advection, and above-normal SSTs over the south-central Pacific Ocean) were also present on 29 May 2019 (Fig. 3). On 30 May 2019, the day of the Los Angeles tornado, the axis of the positively-tilted 500-hPa trough was located approximately 300 km west of Chile (Fig. 4a), and an anomalous surface low (−15 hPa) was centered near 40°S 80°W (Fig. 4c). Flow at 850 hPa over Los Angeles and south-central Chile was from the northwest (Fig. 4b), aiding in the transport of relatively warm and moist air southward (Fig. 4d-e). The SST anomalies remained above normal to the west of Chile (Fig. 4f). As a result of this poleward and eastward transport, CAPE values over south-central Chile and the region extending 300 km offshore to the west were between 200 and 600 J kg^{-1} (Fig. 4d). Given that the mean value of CAPE for this region in late May is between 15 and 45 J kg^{-1} (highest at 1800 UTC and lowest at 0600 UTC; not shown), CAPE values of 600 J kg^{-1} were quite unusual.

The synoptic-scale conditions present on 30 May 2019 (anomalous mid-troposphere troughing, anomalous surface low pressure, positive surface θ_e advection, and low but still above-normal CAPE) are similar to the setups found in other unusual tornado cases, such as Poland (Wrona and Avotniece, 2015), Mexico (Barrett et al., 2017), and the United States (Hales, 1985; Sherburn et al., 2016; King et al., 2017). One factor that is important to mention, and one that may indeed be unique for this particular geographic region, is the potential for the presence of a strong, topographically enhanced low-level jet. Flow blocking by mountains is one of the most prominent effects mountains have on the lower atmosphere (Yu and Smull, 2000), and for the case of the Andes, under certain synoptic-scale conditions, strong low-level flow tends to develop parallel to the terrain axis (Parish, 1982) in

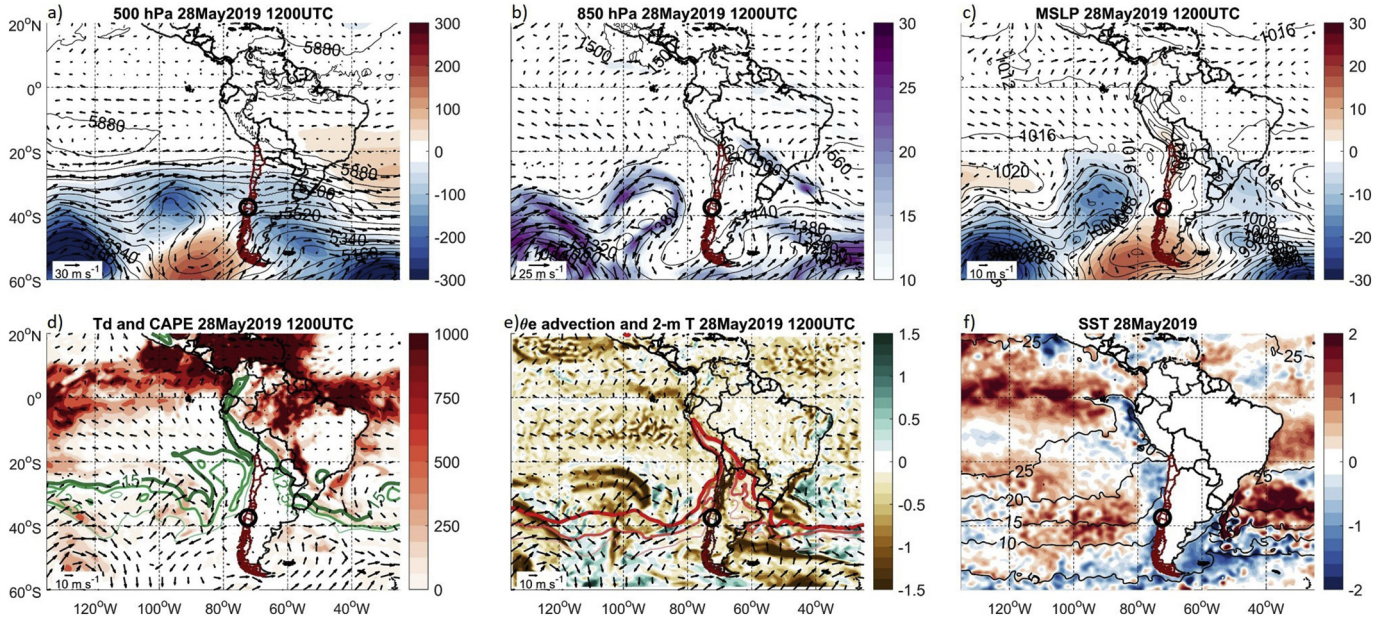

Fig. 2. Synoptic-scale analysis at 1200 UTC 28 May 2019 of (a) 500-hPa wind (vectors) and geopotential height anomalies (in m), (b) 850-hPa wind (vectors) and wind speed anomalies (in m s^{-1}), (c) 10-m wind (vectors) and mean sea level pressure anomalies (in hPa), (d) 2-m dew point temperature (green curves, plotted 10 °C, 12.5 °C, and 15 °C), CAPE (in J kg^{-1}), and 10-m wind (vectors), (e) 2-m temperature (red curves, plotted 10 °C, 12.5 °C, and 15 °C), 10-m wind (vectors), and equivalent potential temperature advection (in C hr^{-1}), and (f) sea surface temperature and anomalies (in °C). All data except SST anomalies come from the Climate Forecast System Reanalysis version 2 (CFSRv2); sea surface temperature anomalies are from NOAA OISST. The black circle on each panel indicates the approximate locations of Los Angeles and Concepción. (For interpretation of the references to color in this figure legend, the reader is referred to the web version of this article.)

response to an ageostrophic acceleration (Marwitz, 1987; Overland and Bond, 1993) in the along-barrier direction (Overland 1984; Lackmann and Overland, 1989). This strong, terrain-enhanced low-level flow can develop in association with cyclonic systems as they approach the Andes (Barrett et al., 2009), and thus can act to significantly enhance levels of low-level SRH and locally increase the probability of tornadogenesis in discrete or semi-discrete convection. For the case of Mechanicsville (New York) tornado, LaPenta et al. (2005) found that the terrain-enhanced low-level flow in eastern New York created an environment that was especially favorable for tornadic supercell development by increasing SRH. The low-level jet in that case also augmented CAPE by advecting warm, moist air poleward. On 30 May 2019, a strong low-level jet (850 hPa wind speeds of 20–25 m s^{-1}) was evident in reanalysis (Fig. 4b) and on regional radiosonde observations (in Santo Domingo, around 300 km to the north, and Puerto Montt, around 500 km to the south) (not shown). Similar barrier jet processes were observed for tornadoes in the Sacramento River valley in California (Hanstrum et al., 2002), in a region topographically and climatologically similar to south-central Chile. Thus, it appears that in this case, a low-level jet was part of the larger synoptic-scale pattern, and flow blocking in the vicinity of Los Angeles could have locally increased the wind speeds in the lower atmosphere to values even greater than

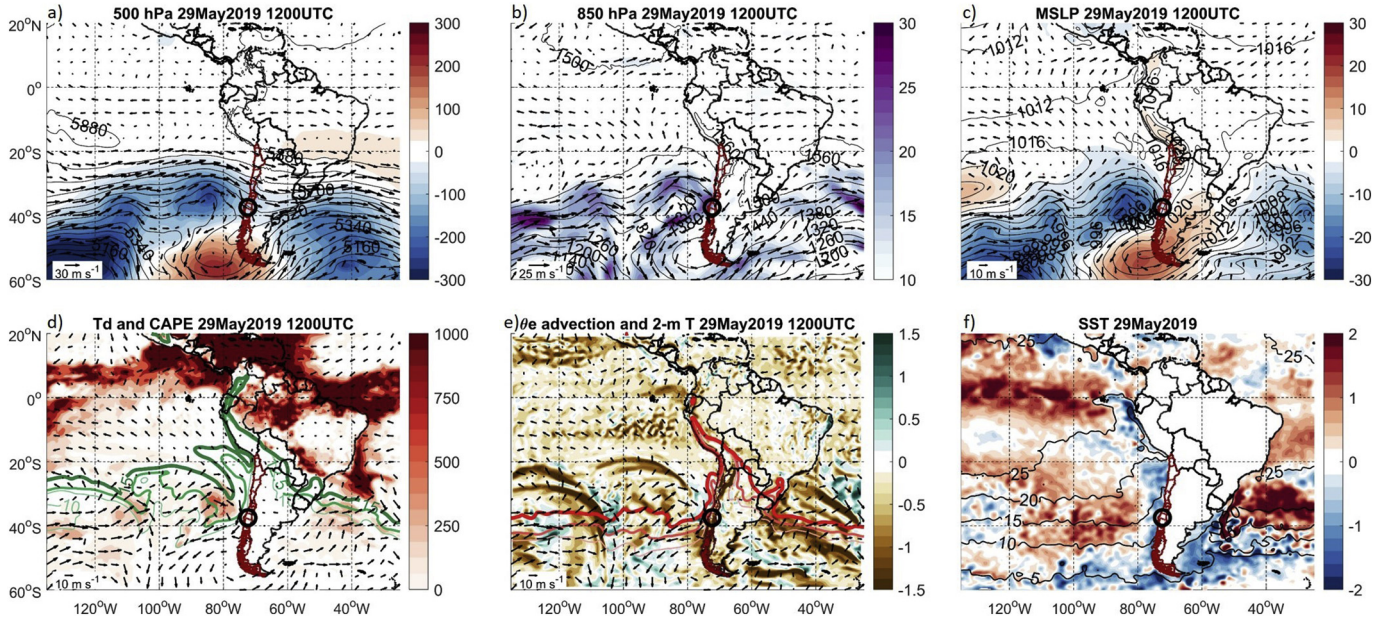

Fig. 3. As in Fig. 2, but for 1200 UTC 29 May 2019.

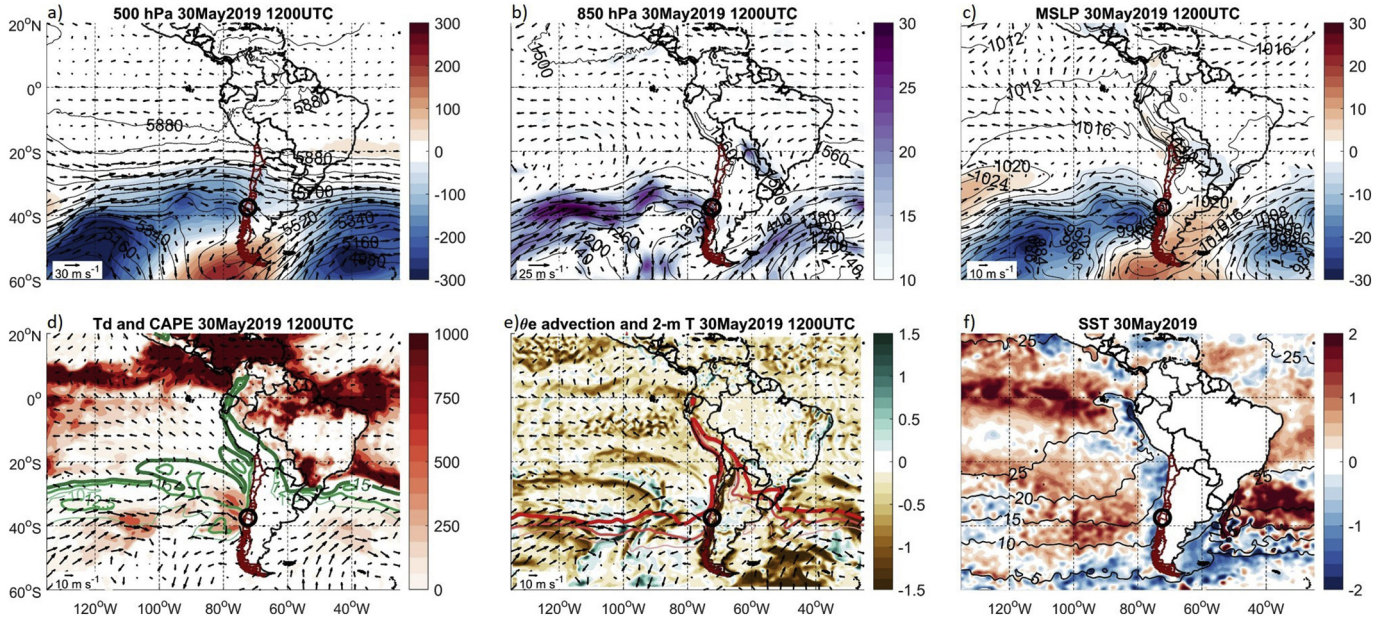

Fig. 4. As in Fig. 2, but for 1200 UTC 30 May 2019.

the synoptic-scale pattern. That possibility of flow enhancement was investigated using output from the WRF model (and results are shared in the next subsection).

The surface conditions observed at Los Angeles indicated a nearly saturated atmosphere throughout the day of 30 May 2019, with air temperatures near 15 °C and dew point temperatures near 14 °C (Fig. 5a). Near the time of the tornado (leftmost vertical brown line in Fig. 5), surface pressures were slowly rising (Fig. 5b), perhaps in response to westward translation of the surface low pressure center closer to the 500-hPa trough axis (and away from Chile). Surface winds were from the northwest between 2.5 and 5 m s^{-1} throughout the day (Fig. 5c), which suggested the presence of low-level and deep-layer shear when paired with 850-hPa winds from the northwest near 20 m s^{-1} (Fig. 4b) and 500-hPa winds from the west near 25 m s^{-1} (Fig. 4a). In the six hours after the tornado occurred (from 1800 local time 30 May 2019 to 0000 local time 31 May 2019), no appreciable change in temperature, dew point temperature, or wind direction or speed was observed (Fig. 5).

Infrared brightness temperatures (Fig. 6a-e) and GLM and WWLLN lightning flashes (Fig. 7a) highlight the cellular nature of the convection in the hours leading up to the tornado in Los Angeles. Brightness temperatures colder than −50 °C were observed in several of the cellular thunderstorms around the time of the tornado (Figs. 6c–e), suggesting that cloud tops reached approximately 10,000 m (or approximately 32,000 ft). Lightning observations confirmed the storm motion (from northwest to southeast), and lightning flash swaths suggested that the storm that produced the tornado in Los Angeles moved from approximately 320° and was accompanied by at least four other nearby

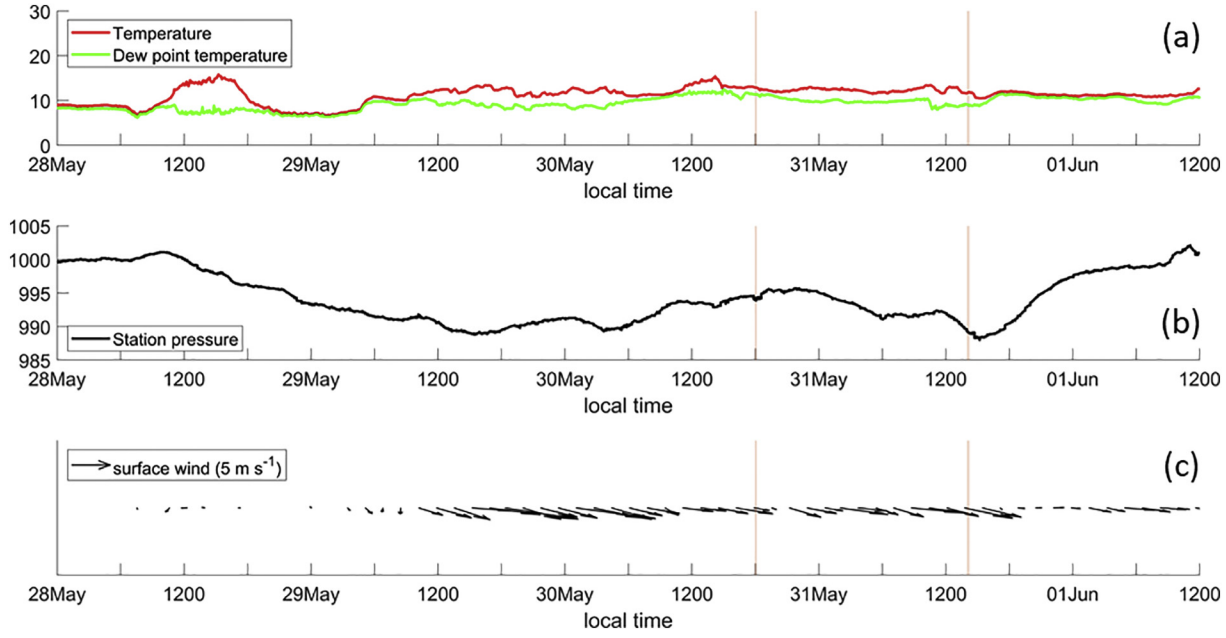

Fig. 5. Time series of (a) 2-m temperature and 2-m dew point temperature (in °C), (b) station pressure (in hPa), and (c) 10-m wind (vectors) at Los Angeles surface observing station, from 0000 28 May 2019 to 1200 01 June 2019. Time is given in local hour (UTC minus 4 h). Vertical thin curves in each panel denote the time of each of the two tornadoes.

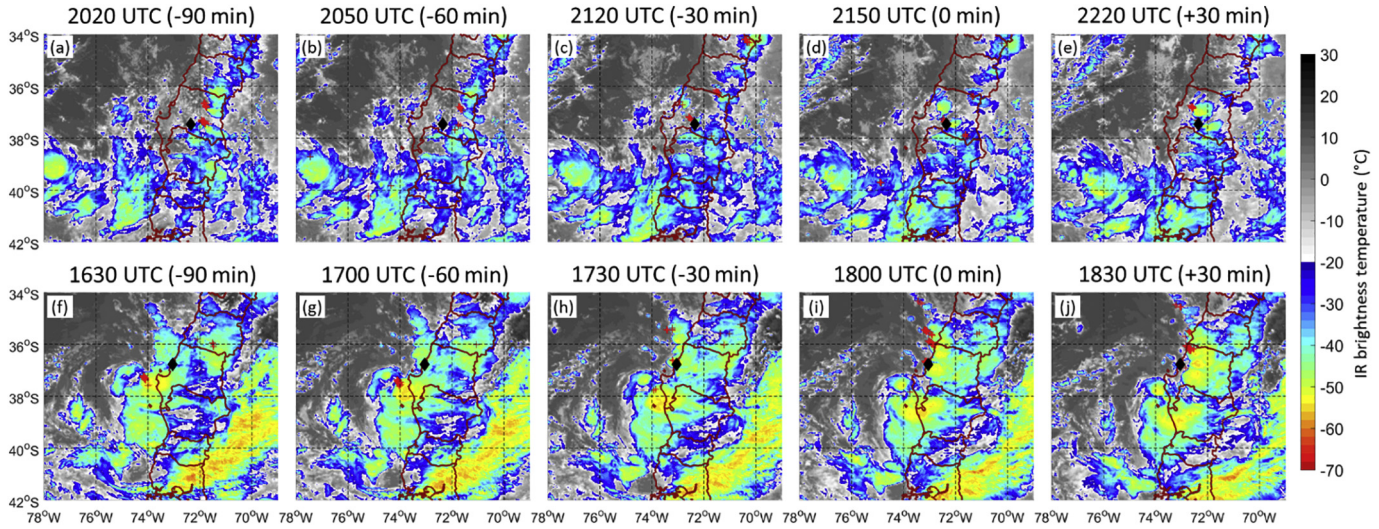

Fig. 6. GOES-16 infrared (IR) brightness temperatures (in °C) for five times: 90, 60, and 30 min before each tornado; the time of each tornado, and 30 min after each tornado. Panels (a)-(e) correspond to the Los Angeles tornado of 30 May 2019, and panels (f)-(j) correspond to the Concepción tornado of 31 May 2019. GLM lightning flashes detected in the 30-min segment leading up to the image time plotted as red + symbols on each panel. Location of each tornado marked by a black diamond. (For interpretation of the references to color in this figure legend, the reader is referred to the web version of this article.)

storms (i.e., within 200 km and 2 h of the Los Angeles tornado). Curiously, the Los Angeles tornado occurred around 2200 UTC, and there are few lightning strikes observed after that time, suggesting the storm weakened just after producing the tornado (e.g., Schultz et al., 2009; Stough et al., 2017). There was also no observed "jump" in lightning occurrence just prior to the tornado.

Synoptic conditions on 31 May 2019 were similar to the conditions observed on 30 May 2019, although the greater coverage of cold IR brightness temperatures (Fig. 6f–j) suggests a greater coverage of convection on 31 May as compared to 30 May. At 500 hPa, a positively tilted trough persisted near 80°W (or 300 km to the west of the coast of south-central Chile; Fig. 8a), and a northwesterly 850-hPa jet (with speeds near 25 m s^{-1}) continued to intersect Chile in the region near Concepción (Fig. 8b). A region of anomalous low pressure (−15 hPa) was centered near 40°S 80°W (Fig. 8c), in a position about 100 km to the east of its position the day before. Positive θ_e advection (Fig. 8e) and a tongue of higher surface temperatures and higher dew point temperatures along the coast supported CAPE values of 200–400 J kg^{-1}, which were 100–200 J kg^{-1} lower than the day before (Fig. 4d) but still 2–4 times larger than the climatological mean value.

Surface conditions in Concepción (Fig. 9) indicated that the surface temperature rose slightly during the morning and early afternoon (from 13° to 15 °C). Dew point temperatures decreased in the morning to near 10 °C, but increased again between 1030 and 1400 local time to near 14 °C (Fig. 9a), supporting positive θ_e advection seen in reanalysis (Fig. 8e). Both temperature and dew point temperature values on 31 May 2019 were similar to 30 May 2019. Surface pressures fell from around 9 pm local time 30 May 2019 until the time of the tornado (2 pm local time 31 May; Fig. 9b), indicating the approach of the synoptic-scale surface low. Pressures rose immediately following the tornado, and wind direction changed subtly to the northwest, possibly associated with the passage of a mesohigh in the wake of the mesoscale convective system (Johnson, 2001) or with the passage of the surface pressure trough. Surface winds were stronger on 31 May 2019 (nearly 10 m s^{-1}) and from the north-northeast (compared to < 5 m s^{-1} in Los Angeles and from the northwest). The stronger and more backed surface winds were possibly the result of greater terrain-induced flow blocking and the strengthening of a barrier jet (Viale and Nuñez, 2011) as the upper trough approached, a factor that would have been more prominent on 31 May than on 30 May. These conditions indicate that low-level and deep-layer vertical wind shear were higher in Concepción on 31 May 2019, while CAPE values were higher in Los Angeles on 30

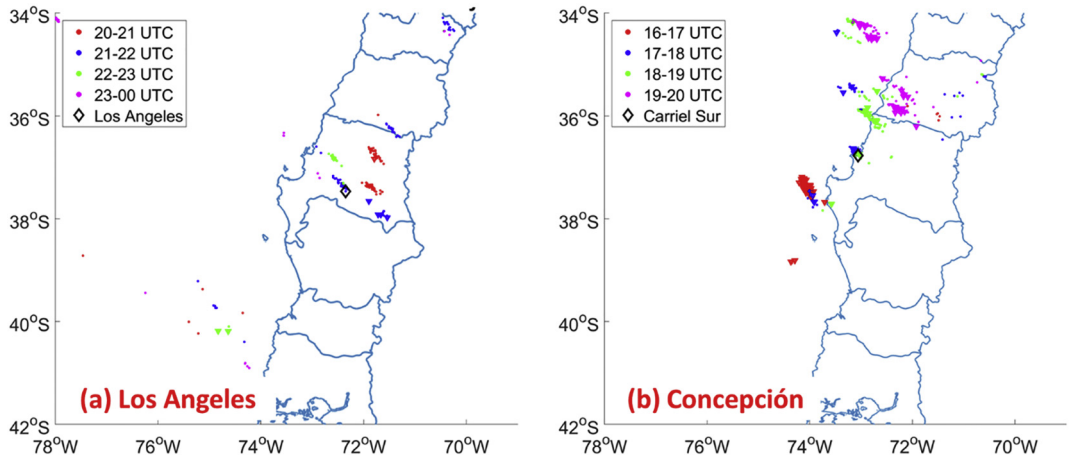

Fig. 7. GLM (circles) and WWLLN (triangles) lightning flashes detected from (a) 2000–0000 UTC 30 May 2019, and (b) 1600–2000 UTC 31 May 2019. Location of each tornado marked by an open diamond.

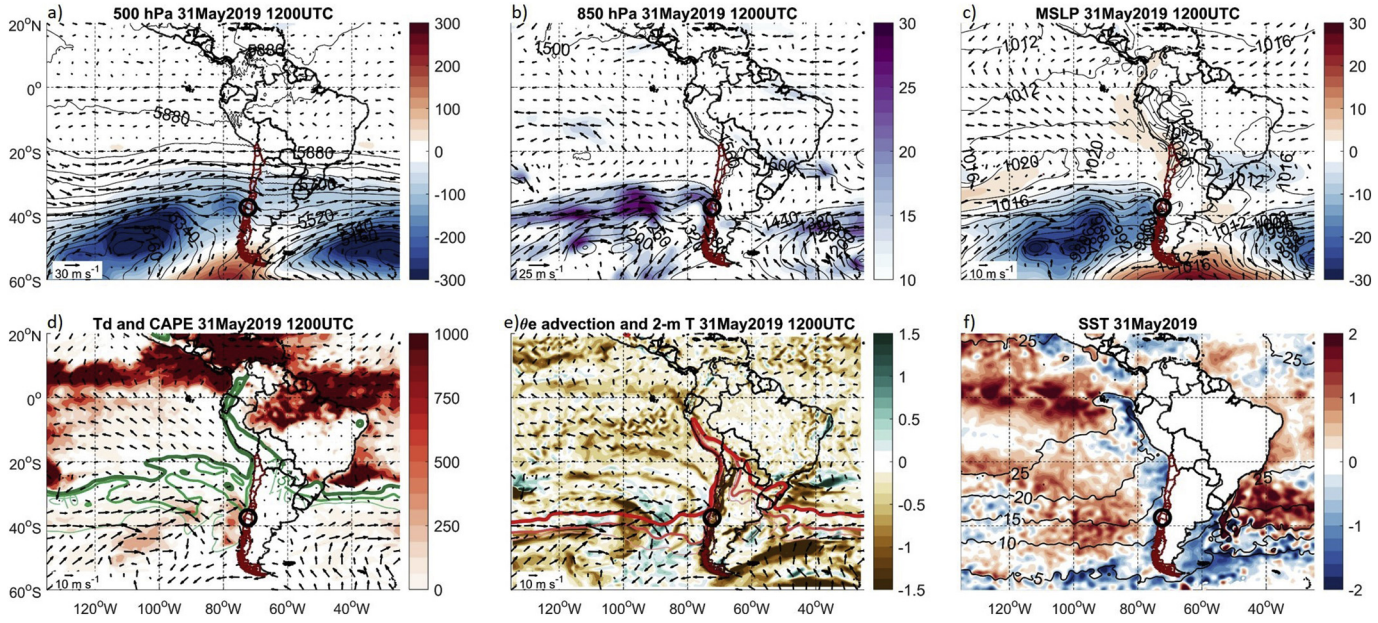

Fig. 8. As in Fig. 2, but for 1200 UTC 31 May 2019.

May 2019. Those ingredients are examined in more detail in the following section using output from the WRF model.

IR brightness temperatures (Fig. 6f–j) were overall 5–10 °C colder on 31 May 2019 than on 30 May 2019, suggestive of cloud tops nearer 11,000 m (36 000 ft). Thus, even though the overall surface temperatures and dew point temperatures on 31 May 2019 were slightly cooler, and CAPE values slightly lower, the colder brightness temperatures support the argument for vigorous deep convection, perhaps even more vigorous than on 30 May 2019. Furthermore, the coverage of cold brightness temperatures near the time of the tornado (Fig. 6h–j) suggests that the tornadic thunderstorms could have been embedded in a larger convective system. Indeed, at the time of the Concepción tornado (Fig. 6i), the city was located on the northwest edge of a thunderstorm with high brightness temperature gradient, a characteristic that has been associated with local thunderstorm severity (Bedka et al., 2010).

In addition, the overall coverage and linear nature of lightning flash locations in the several hours leading up to the tornado (Fig. 7b) supports the idea that storms were semi-discrete with an overall movement to the southeast. Lightning flash swaths indicate a storm motion from 330° (Fig. 7b). This pattern is similar between the two days, suggesting the two tornadoes formed in similar synoptic-scale conditions.

3.2. Mesoscale conditions during each tornado

Output from a high-resolution simulation from the WRF model was analyzed to better understand the mesoscale conditions present during each tornado. Before analyzing those conditions, model radar reflectivity (at the lowest model sigma level, closest to the surface) was examined and compared to IR satellite at the corresponding time (Chile does not yet have operational weather radar). On 30 May 2019, WRF

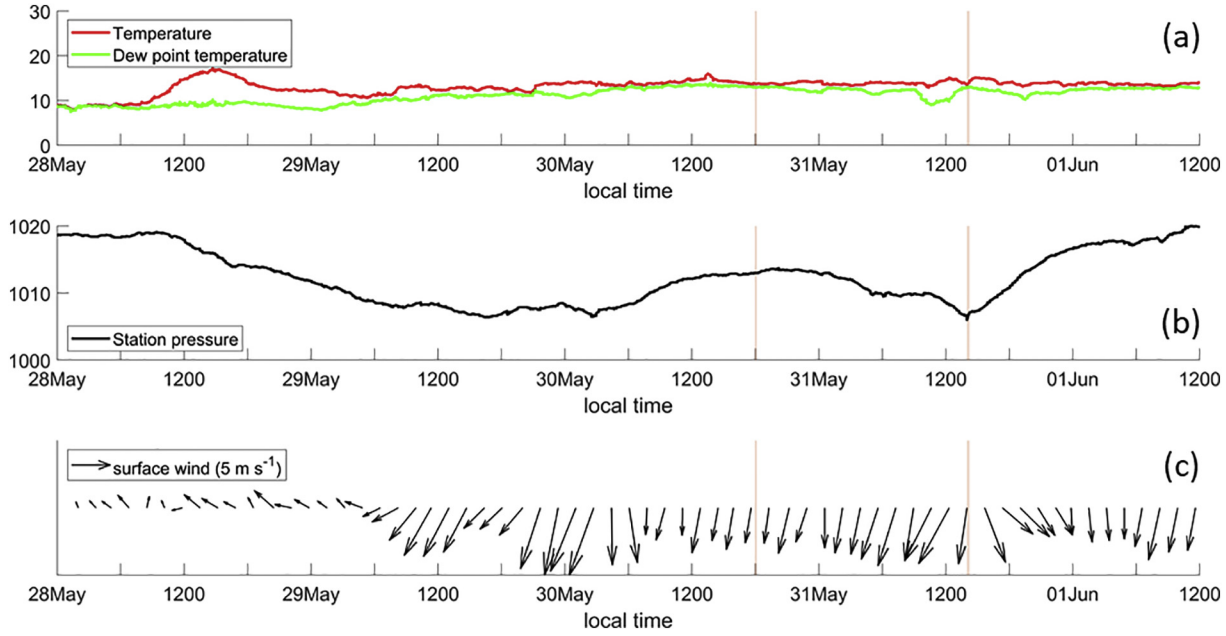

Fig. 9. As in Fig. 5, but for the Concepción observing station.

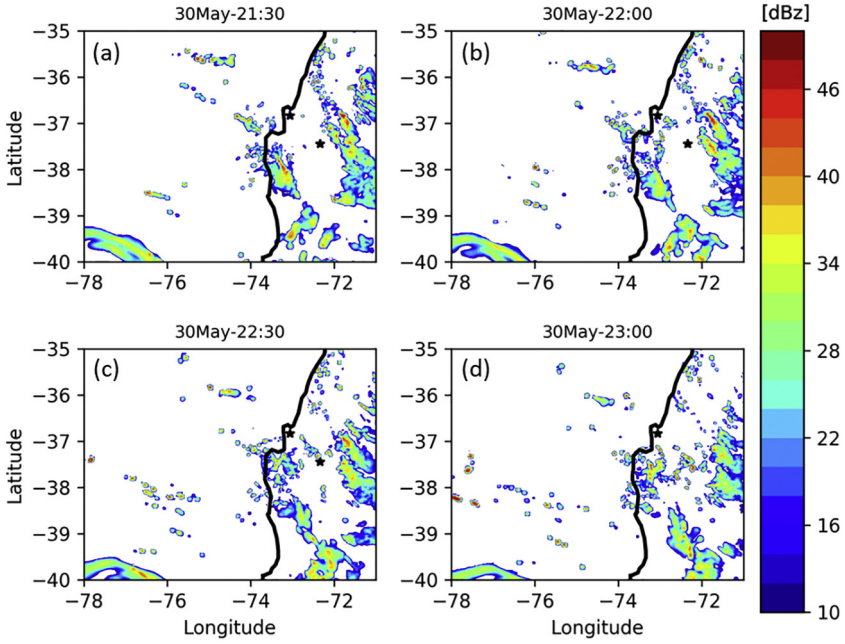

Fig. 10. Simulated radar reflectivity (in dBZ) at WRF sigma level closest to the surface for (a) 2130 UTU, (b) 2200 UTC, (c) 2230 UTC, and (d) 2300 UTC 30 May 2019. Black stars in each panel indicate the cities of Los Angeles and Concepción, respectively.

model reflectivity at 2130 UTC (about 30 min prior to the tornado) showed two broad regions of linear-structure convection, one about 100 km to the northeast of Los Angeles and the other about 200 km to the southwest of Los Angeles (Fig. 10a; Los Angeles is indicated by the easternmost marker in the figure). Smaller, cellular convection was present to the northwest of the linear elements. IR satellite at 2120 UTC also featured deep convection to the northeast of Los Angeles (Fig. 6c), but the satellite signature suggests the convection was more cellular, and closer to Los Angeles than indicated in the WRF simulation. At 2150 UTC, the tornadic thunderstorm is seen in IR imagery over the city of Los Angeles (Fig. 6d), while WRF simulation has just initiated convection 10 km to the southeast of Concepción (Fig. 10b). At 2220 UTC, IR satellite imagery indicates cellular convection to the east-southeast and north-northwest of Los Angeles (Fig. 6e), while the WRF simulation at 2230 UTC (Fig. 10c) has cellular convection with maximum reflectivity over 45 dBZ approximately 10 km to the north of Los Angeles. This convection intensified in the model, and by 2300 UTC (Fig. 10d), the WRF simulation has a small, curved convective element over Los Angeles with a shape similar to the "kidney bean" structure mentioned by others (Moller et al., 1990; Doswell III, 1998; Parker, 2010) that can be suggestive of supercell characteristics. Furthermore, maximum simulated updraft helicity in the 2–5-km layer on 30 May 2019 showed several southeastward-moving swaths (Fig. 11a), suggestive of at least transient updraft rotation in the stronger convective elements. Moreover, for cold-season convection, a shallower updraft helicity layer (perhaps 1–3 km) may be more appropriate than the 2–5-km layer, although that was not tested here. Thus, while the timing was approximately 1 h delayed, the WRF simulation produced discrete, cellular (and suggestive of supercellular) convective elements near the city of Los Angeles on the afternoon of 30 May 2019, with structure, coverage, and motion similar to IR satellite observations.

As mentioned earlier, the convective evolution of 31 May 2019 was more complex than 30 May 2019, due to the more widespread nature of the convection. IR imagery (Fig. 6g–j) from 60 min prior to the tornado to 30 min after the tornado suggest that convection was loosely organized in linear and mesoscale convective system (MCS) structures, with the tornadic convective element in Concepción located on the trailing (northwest) fringe of the MCS as it moved from over water to over land. The WRF simulation captured this evolution relatively well in both

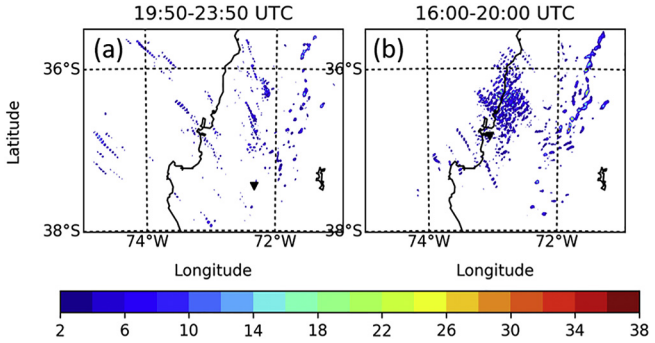

Fig. 11. Maximum model updraft helicity (color shaded; $m^2\ s^{-2}$) for (a) 1950–2350 UTC 30 May 2019 and (b) 1600–2000 UTC 31 May. Black triangles in each panel indicate the cities of Los Angeles and Concepción, respectively.

timing and space. For example, at 1700 UTC, one hour prior to the tornado, the WRF simulation featured a curved line of broken convective cells up to 100 km north and northwest of Concepción (Fig. 12a). By 1730 UTC, the simulated convection had moved closer to the coast, with individual convective elements remaining on the northwestern fringe of the overall MCS (Fig. 12b). At 1800 UTC, the WRF simulation featured a broken line of semi-discrete convective cells extending in a north-south line approaching Concepción (Fig. 12c). Between 1800 and 1830 UTC, the model moved the line to the east, while individual cells moved south-southeast (Fig. 12d). Furthermore, simulated updraft helicity in the 2–5-km layer showed many southeastward-moving swaths (Fig. 11b), suggestive of updraft rotation in many of the convective elements. This evolution compares well with IR imagery and lightning observations, suggesting that the WRF model also reproduced reasonably well the convective processes on 31 May 2019.

Based on the WRF simulation, the mesoscale ingredients present on 30 May 2019 at the time of the tornado (2150 UTC) included the following: (1) a strong north-northeasterly surface wind (4.4 m s^{-1}) associated with an area of surface low pressure 500 km to the southwest (Fig. 13a); (2) 0–3-km SRH of $-253\ m^2\ s^{-2}$ (values are negative because the cyclonic rotation is in the Southern Hemisphere; Fig. 13b); (3)

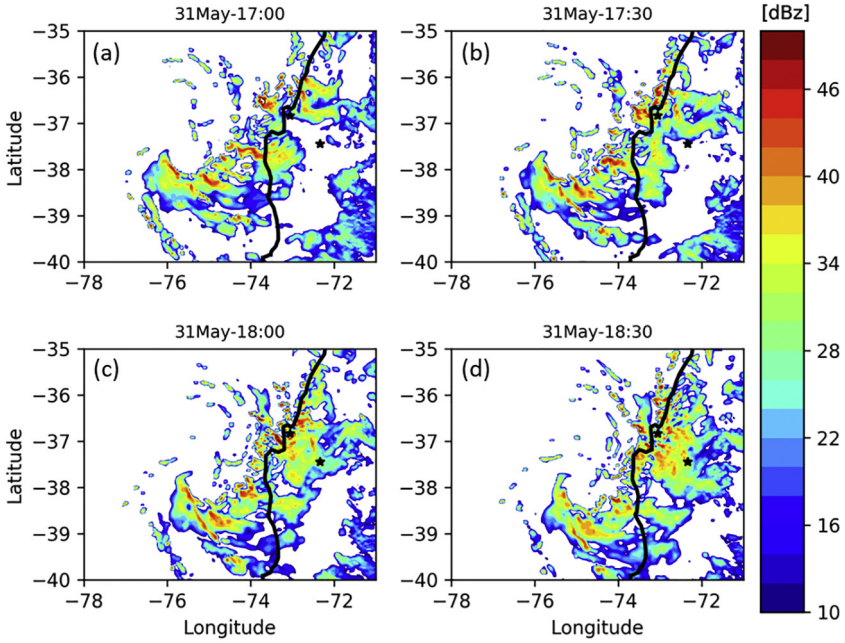

Fig. 12. Same as Fig. 10 but for (a) 1700 UTC, (b) 1730 UTC, (c) 1800 UTC, and (d) 1830 UTC 31 May 2019.

LCL height of 713 m (Fig. 13c); (4) surface to 900 hPa shear (an approximation of the 0–1-km shear) of 13 m s^{-1} (Fig. 13d); (5) surface-based CAPE of 163 J kg^{-1} (Fig. 14a); and (6) surface to 500 mb shear (an approximation of the 0–6-km bulk shear) of 13.0 m s^{-1} (Fig. 14c). To avoid possible convective contamination, those values are reported by averaging nine model grid points surrounding Los Angeles with dBZ < 20.

The overall mesoscale ingredients present at the time of the tornado (1800 UTC) on 31 May 2019 were similar to 30 May, in that both featured "low-CAPE, high-shear" environments, but 31 May 2019 featured lower CAPE and higher shear. The surface low pressure was < 100 km from Concepción (Fig. 15a), with higher values of 0–3-km SRH (−688 vs −253 m^2 s^{-2}) (Fig. 15b), 0–1-km shear (17 vs 13 m s^{-1}) (Fig. 15d), and 0–6-km shear (21.4 vs 13 m s^{-1}) (Fig. 14d). The WRF simulated CAPE values at the nine non-convectively contaminated grid points around the tornado location on 31 May 2019 were lower than on 30 May (Fig. 14a-b), but in both simulations, reservoirs of CAPE approaching 1000 J kg^{-1} were located < 100 km from each city. These reservoirs of higher CAPE were also located in the regions where convective initiation occurred on each day.

The mesoscale conditions on each day were very similar to the low-CAPE (≤ 500 J kg^{-1}), high-shear environments (deep-layer bulk shear ≥18 m s^{-1} and low-level bulk shear ≥10 m s^{-1}) identified by others as favorable for cool-season tornadoes (Hanstrum et al., 2002; Davies, 2006; Guyer et al., 2006; Schneider et al., 2006; Brooks, 2009; Sherburn and Parker, 2014; Mulder and Schultz, 2015; Sherburn et al., 2016; King et al., 2017; Childs et al., 2018). Even though SSTs were 0.5–1 °C below normal adjacent to the coast (Figs. 2f, 3f, 4f, and 8f), WRF simulated reflectivity suggests that the temperature difference between relatively warm water (14–15 °C) and cold air aloft in the trough may have helped increased updraft intensity by steepening low-level lapse rates, particularly for post-frontal convection forming offshore and

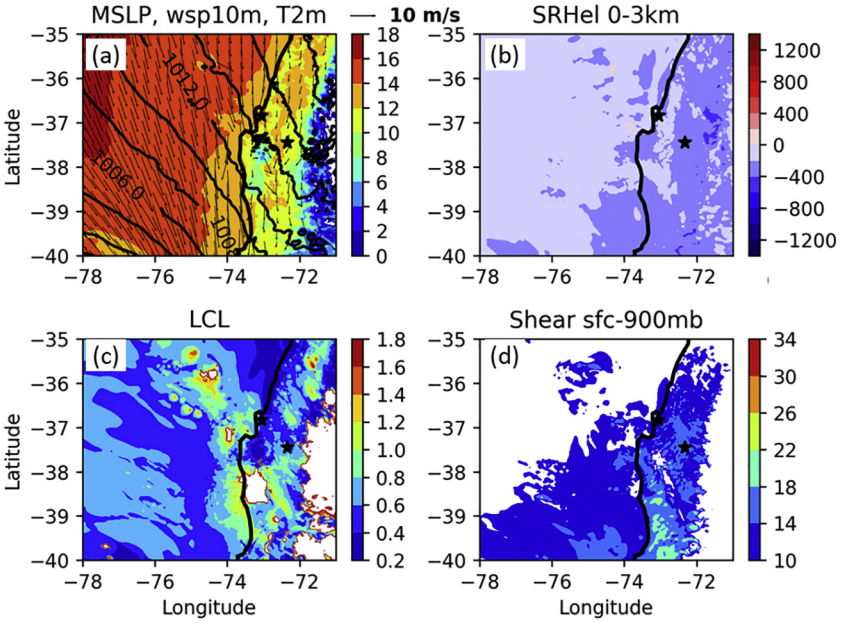

Fig. 13. WRF simulated (a) mean sea level pressure (contours, in hPa), 2-m dew point (color shading, in °C), and 10-m wind (vectors), (b) 0–3 km storm-relative helicity (in m^2 s^{-2}), (c) surface-based lifting condensation level (in km), and (d) surface-900 hPa (approximately 0–1 km) bulk wind difference (in m s^{-1}), valid at 2150 UTC 30 May 2019. Both Los Angeles and Concepción are marked with a black star in each panel.

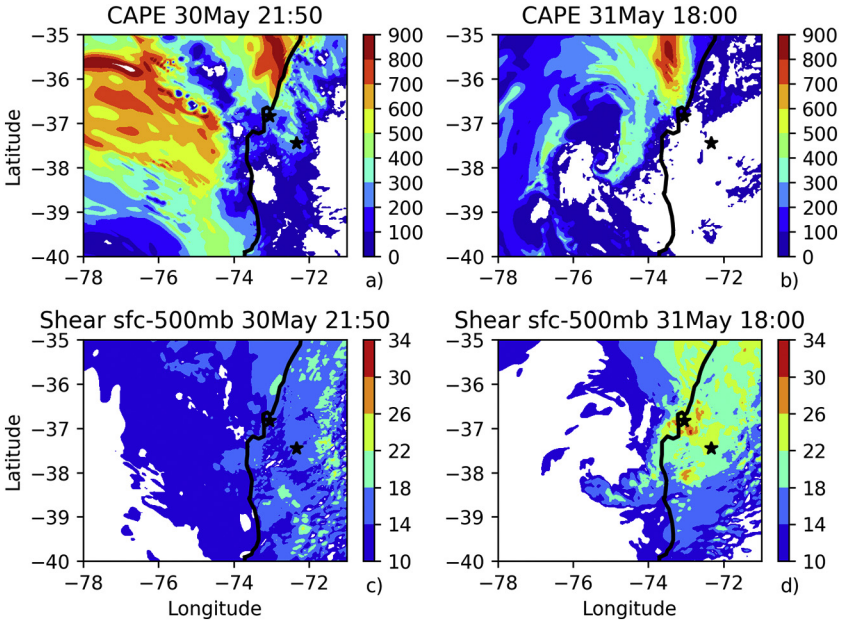

Fig. 14. (a)-(b) CAPE (in J kg^{-1}) and (c)-(d) surface-to-500 hPa bulk wind difference (in m s^{-1}), valid at 2150 UTC 30 May 2019 and 1800 UTC 31 May 2019, respectively. Both Los Angeles and Concepción are marked with a black star in each panel.

moving onshore. A similar process was suggested by Sioutas and Keul (2007) for tornadoes moving onshore from the Ionian Sea. This is also similar to the enhancement of tornado activity by relatively warm SSTs found by Hales (1985) for tornadoes in Los Angeles, California. The role of SST in providing or enhancing the environment favorable for these Chilean tornadoes was not further examined in this study, and is suggested as an area for future work.

Finally, output from the WRF simulation indicates a southward low-level jet over the region as the synoptic-scale cyclone approached (Fig. 16). Meridional winds in the 900–700-hPa layer near the time of each tornado were approximately 10 m s^{-1} on 30 May (Fig. 16b) and in excess of 20 m s^{-1} on 31 May (Fig. 16e) (both from the north), and those strong winds extended from the coastline eastward to the Andes cordillera. The horizontal structure of the northerly jet, with an increase in magnitude from west to east and a maximum immediately upstream of the topography (Fig. 16b,e), suggests flow blocking by the Andes (Viale and Norte, 2009). The low-level jet is also evident up to 200 km offshore (west) of Chile, suggesting that the jet was likely a combination of synoptic-scale factors (associated with the surface cyclone) and mesoscale factors (associated with flow blocking). This low-level jet was important in increasing the low-level environmental helicity during each tornado, but was not investigated further in this study. The role of the low-level jet and its interaction with the topography is suggested as an area for future study.

3.3. The subseasonal context

The subseasonal context was the final element examined of this two-day tornado event in south-central Chile. It is well known that the tropical MJO has significant impacts in South America during the

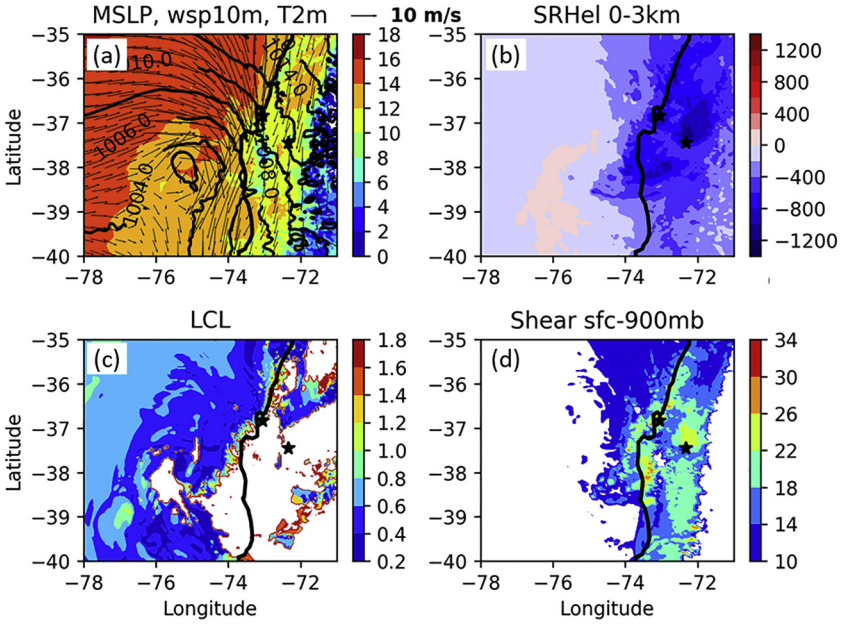

Fig. 15. As in Fig. 12, but valid at 1800 UTC 31 May 2019.

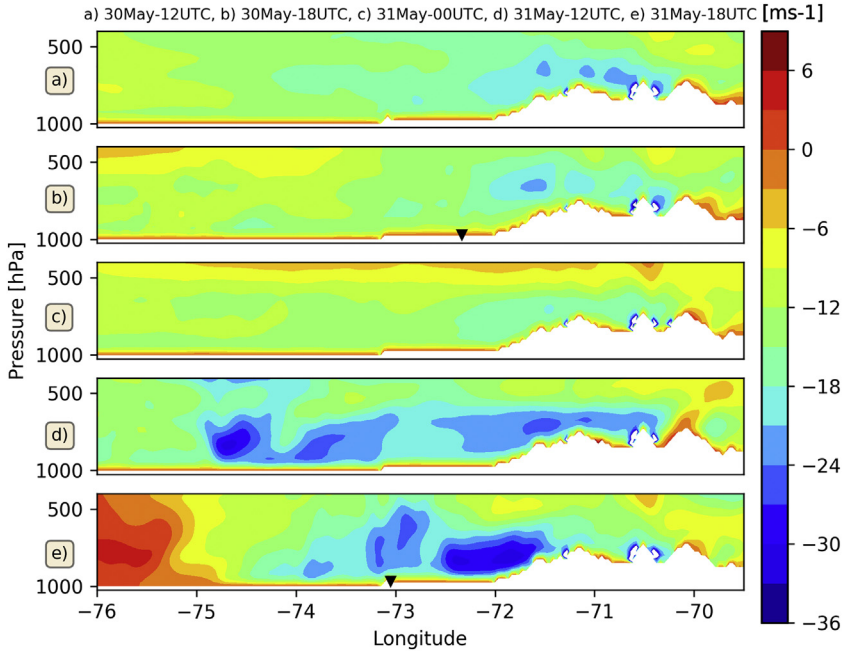

Fig. 16. WRF simulated meridional (v) wind component along a vertical west-east cross section from 76°W to 69.5°W along 37°S, valid at (a) 1200 UTC 30 May, (b) 1800 UTC 30 May, (c) 0000 UTC 31 May, (d) 1200 UTC 31 May, and (e) 1800 UTC 31 May.

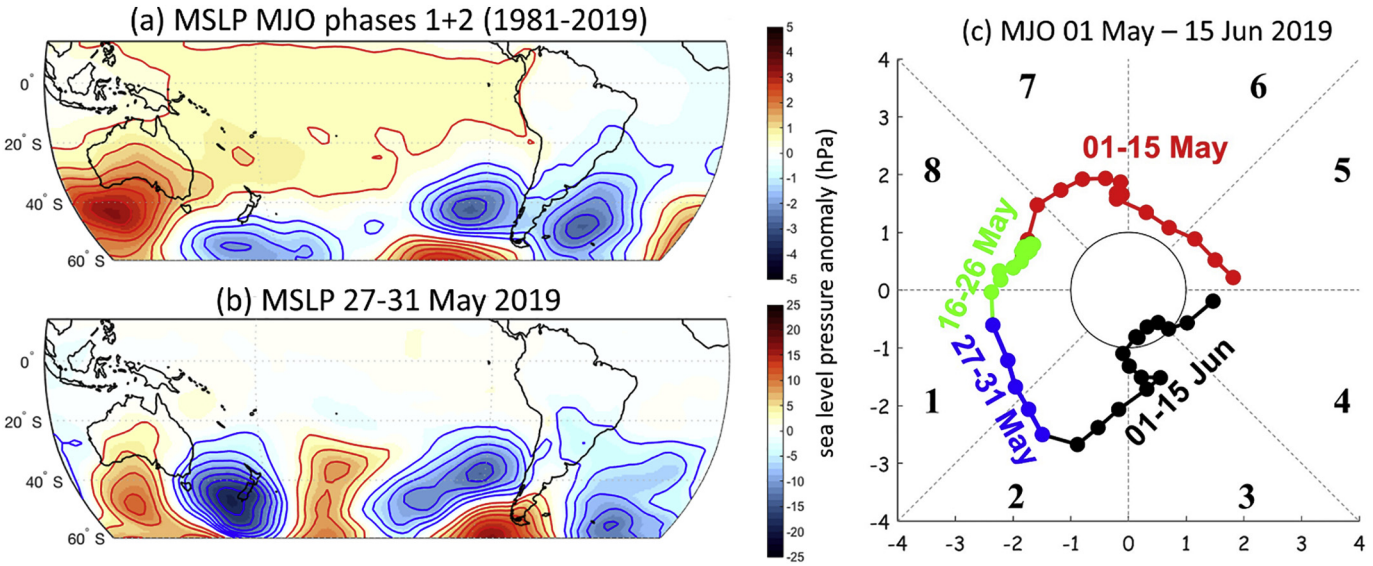

Fig. 17. Composite anomalies of sea level pressure (in hPa) for (a) MJO phases 1 and 2 for all May and June months from 1981 to 2019 (256 days for phase 1 and 205 days for phase 2), and (b) 27–31 May 2019. (c) phase of the Real-time Multivariate MJO index from 01 May 2019 to 15 June 2019.

austral winter, both via effects from the propagatign MJO itself (Alvarez et al., 2016; Grimm, 2019) and teleconnections stemming from Rossby wave trains propagating from Eastern Hemisphere convective heating sources (Barrett et al., 2012b; Juliá et al., 2012; Jacques-Coper et al., 2015; Rondanelli et al., 2019). From May to June 2019, a very to extremely active MJO event (following the definition of LaFleur et al., 2015) moved from the Indian Ocean, through the Maritime Continent and western Pacific Ocean, and into the Western Hemisphere (Fig. 17c). The time-averaged MSLP anomalies for 27–31 May 2019 (Fig. 17b) resembled composite anomalies for MJO phases 1 and 2 for the months of May and June 1981–2019 (Fig. 17a). (Phases 1 and 2 were selected for comparison because the tornadoes occurred while the MJO was in those phases; Fig. 17c). In particular, in both the climatological (Fig. 17a) and observed (Fig. 17b) MSLP fields, anomalous low pressure can be seen to the west of Chile as part of a large-scale wave pattern across the South Pacific. Furthermore, time-averaged anomalies of both 500-hPa height (Fig. 18b) and 2-m dew point temperature (Fig. 18d) for 27–31 May 2019 also resembled composite anomalies for MJO phases 1 and 2 for May and June 1981–2019 (Fig. 18a and c). This agreement suggests that the surface low pressure, 500-hPa trough, and increased surface moisture that were associated with the tornadoes of 30–31 May 2019 are all an expected part of the subseasonal atmospheric evolution during MJO phases 1 and 2 in the months of May and June. Similar results were obtained with corresponding fields of the reanalysis lifted index (not shown). Furthermore, the 500-hPa wave train (Fig. 18b) was similar to the ray tracing found by Rondanelli et al. (2019), indicating that the evolution of the large-scale tropospheric circulation over the second half of May 2019 was at least partly associated with the strong MJO event in progress.

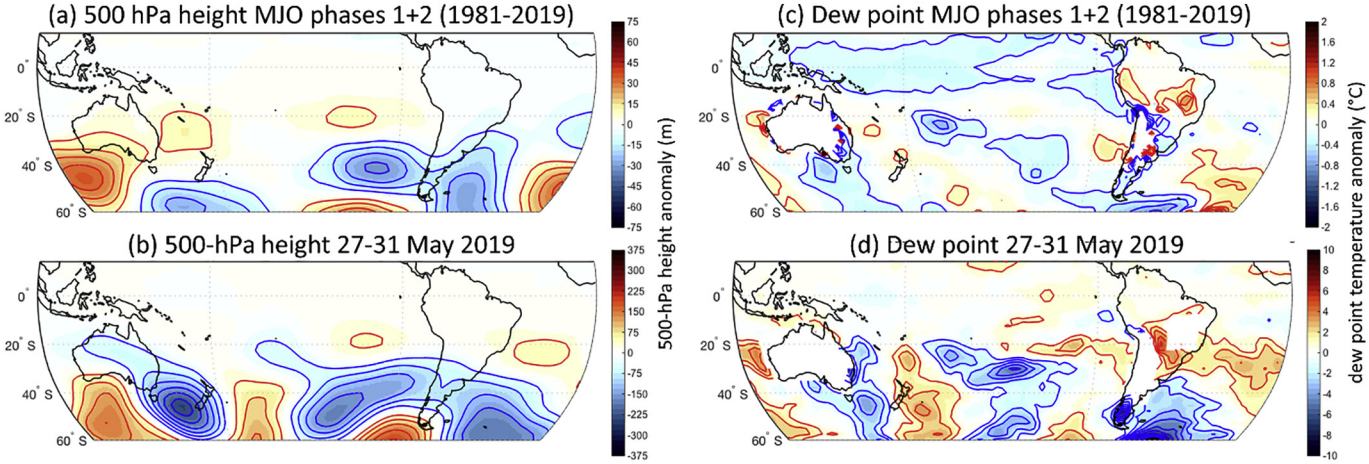

Fig. 18. As in Fig. 17, but for composite anomalies of (a)-(b) 500-hPa height and (c)-(d) 2-m dew point temperature.

4. Conclusions and discussion

On consecutive days in late May 2019, tornadoes occurred in the cities of Los Angeles and Talcahuano/Concepción in south-central Chile. The main goal of this study was to examine the two-day event from (1) the synoptic-scale, using reanalysis data and surface observations; (2) the mesoscale, using satellite observations and a high-resolution regional NWP model; and (3) the subseasonal scale, using time-averaged and historical composite analyses. The synoptic pattern evolution featured an anomalous mid-troposphere trough at 500 hPa to the west of Chile, with a cyclonic low-level jet centered near 850 hPa and surface low pressure located along the coast. Surface and lower-tropospheric winds from the north-northeast, north, and north-northwest aided in establishing a humid air mass associated with positive θ_e advection on the days leading up to each tornado. Above-normal values of CAPE, of order 500 J kg^{-1} (higher on 30 May and lower on 31 May), were associated with each tornado. Similarly high values of low-level (0–1-km) and deep layer (0–6-km) bulk shear (near 15 m s^{-1} on 30 May and 20 m s^{-1} on 30 May), and high values of 0–3-km SRH (-300 m^2 s^{-2} on 30 May and -800 m^2 s^{-2} on 31 May), were also present on each day. Finally, low LCLs, lower than 650 m, were present each day. All of those parameters agree well with studies that have examined tornado formation in “low CAPE-high shear” environments.

Given the mesoscale parameter space, IR satellite evolution, lightning patterns, and simulated WRF reflectivity and updraft helicity on both days, the evidence suggests that both of these tornadoes were likely products of supercell thunderstorms. Storm motion estimated from lightning flash swaths on 30 May was from 320°, while on 31 May it was from 330°, suggesting similar synoptic steering conditions. Indeed, calculations using the Bunkers et al. (2000) technique for left-moving supercells gave storm motion estimates of 295–305° on 30 May and 300–320° on 31 May; the agreement between the Bunkers method and observed lightning swaths and WRF simulated reflectivity and helicity suggests that the storms on both days were supercellular.

The threats posed by supercell thunderstorms (strong winds, large hail, and tornadoes) were perhaps not seriously considered by forecasters for the marine-like climate zones of Chile prior to 2019 (i.e., Brooks et al., 2003). Thus, an important result from this paper is that forecasters should be aware of the possibility for thunderstorm rotation and tornadoes when the synoptic and mesoscale parameters resemble those seen on 30 and 31 May 2019. Additionally, the WRF simulation results indicate that CAPE values approaching 1000 J kg^{-1} were located just offshore of Chile, perhaps connected to anomalously warm sea surface temperatures either offshore of Chile or to the bay region of Concepción (not shown). Furthermore, the Andes topography may have played an important role in changing the orientation and enhancing the speeds of the low-level jet via flow blocking, on both days but particularly on 31 May 2019, when wind speeds in the lower troposphere just above the surface (up to about 700 mb) were high in both reanalysis and the WRF simulation. This modulation would agree with Viale and Norte (2009), who found that flow blocking in central Chile acts to increase winds speeds in the lower troposphere, from just above the surface up to about 700 hPa. These greater winds thereby likely increased shear values in the vicinity of both Los Angeles and Concepción. A more robust examination of the contribution of SST anomalies and flow blocking by the Andes to the conditions that favored these tornadic thunderstorms is suggested as future work.

Another important result of this study is to highlight potential connections between this event and the larger scale, low-frequency evolution of the atmosphere. The anomalous 500-hPa trough to the west of south-central Chile played an important role creating conditions favorable for the development of the tornadoes, and the surface pressure and 500-hPa height patterns of late May 2019 were similar to the historical pressure and height composites for MJO phases 1 and 2 during the months of May–June. Furthermore, the 500-hPa wave pattern was similar to the ray paths found by Rondanelli et al. (2019) for MJO-driven teleconnections in Chile. Given that the slower-evolving MJO now has predictability out to 3–4 weeks (Lim et al. 2018), it thus seems possible to anticipate some extreme events beyond the typical synoptic time window of 8–10 days (Grazzini and Vitart, 2015; Weber and Mass, 2019). Thus, future work is suggested to link extreme synoptic-scale events, including in Chile, to slower-evolving, larger scale processes.

Declaration of Competing Interest

The authors declare that they have no known competing financial interests or personal relationships that could have appeared to influence the work reported in this paper.

Acknowledgments

The authors wish to thank the World Wide Lightning Location Network (http://wwlln.net), a collaboration among over 50 universities and institutions, for providing the lightning location data used in this paper. NOAA High Resolution SST data were provided by the NOAA/OAR/ESRL PSD, Boulder, Colorado, USA, from their Web site at https://www.esrl.noaa.gov/psd/.

Funding

This work was supported by Conicyt [grant number MEC80180038]

and the Office of Naval Research [grant number N0001416WX01752]. JCM acknowledges financial support from Centro de Estudios Atmosféricos y Astroestadística (CEAAS), Universidad de Valparaíso. Powered@NLHPC: This research was partially supported by the supercomputing infrastructure of the National Laboratory for High Performing Computer (ECM-02). MJC thanks the funding provided by FONDAP/CONICYT 15110009, FONDECYT/CONICYT 11170486, and PAI/CONICYT 79160105.

References

Allen, J.T., Karoly, D.J., 2014. A climatology of Australian severe thunderstorm environments 1979–2011: inter-annual variability and ENSO influence. Int. J. Climatol. 34, 81–97. https://doi.org/10.1002/joc.3667.

Alvarez, M., Vera, C., Kiladis, G., Liebmann, B., 2016. Influence of the Madden Julian Oscillation on precipitation and surface air temperature in South America. Clim. Dyn. 46, 245–262. https://doi.org/10.1007/s00382-015-2581-6.

Baggett, C.F., Nardi, K.M., Childs, S.J., Zito, S.N., Barnes, E.A., Maloney, E.D., 2018. Skillful subseasonal forecasts of weekly tornado and hail activity using the Madden-Julian Oscillation. J. Geophys. Res. Atmos. 123, 12661–12675.

Barrett, B.S., Gensini, V.A., 2013. Variability of central United States April–May tornado day likelihood by phase of the Madden-Julian Oscillation. Geophys. Res. Lett. 40, 2790–2795.

Barrett, B.S., Garreaud, R.D., Falvey, M., 2009. Effect of the Andes cordillera on precipitation from a midlatitude cold front. Mon. Weather Rev. 137, 3092–3109. https://doi.org/10.1175/2009MWR2881.1.

Barrett, B.S., Fitzmaurice, S.J., Pritchard, S.R., 2012a. Intraseasonal variability of surface ozone in Santiago, Chile: modulation by phase of the Madden-Julian Oscillation (MJO). Atmos. Environ. 55, 55–62. https://doi.org/10.1016/j.atmosenv.2012.04.040.

Barrett, B.S., Carrasco, J.F., Testino, A.P., 2012b. Madden-Julian Oscillation (MJO) modulation of atmospheric circulation and Chilean winter precipitation. J. Clim. 25, 1678–1688.

Barrett, B.S., Farfán, L.M., Raga, G.B., Hernández, D.H., 2017. The unusual early morning tornado in Ciudad Acuña, Coahuila, Mexico of 25 May 2015. Mon. Weather Rev. 145, 2049–2069. https://doi.org/10.1175/MWR-D-16-0252.1.

Bedka, K., Brunner, J., Dworak, R., Feltz, W., Otkin, J., Greenwald, T., 2010. Objective satellite-based detection of overshooting tops using infrared window channel brightness temperature gradients. J. Appl. Meteorol. Climatol. 49, 181–202. https://doi.org/10.1175/2009JAMC2286.1.

Bolton, D., 1980. The computation of equivalent potential temperature. Mon. Weather Rev. 108, 1046–1053. https://doi.org/10.1175/1520-0493(1980)108<1046:TCOEPT>2.0.CO;2.

Brooks, H.E., 2009. Proximity soundings for severe convection for Europe and the United States from reanalysis data. Atmos. Res. 93, 546–553. https://doi.org/10.1016/j.atmosres.2008.10.005.

Brooks, H.E., Lee, J.W., Craven, J.P., 2003. The spatial distribution of severe thunderstorm and tornado environments from global reanalysis data. Atmos. Res. 67–68, 73–94.

Brooks, H.E., Anderson, A., Riemann, K., Ebbers, I., Flachs, H., 2007. Climatological aspects of convective parameters from the NCAR/NCEP reanalysis. Atmos. Res. 83, 294–305.

Brooks, H.E., Doswell III, C.A., Zhang, X., Chernokulsky, A., Tochimoto, E., Hanstrum, B., Nascimento, E., Sills, D.M.L., Antonescu, B., Barrett, B.S., 2019. A century of progress in severe convective storm research and forecasting. Meteorol. Monogr. 59, 18.1–18.41. https://doi.org/10.1175/AMSMONOGRAPHS-D-18-0026.1.

Bunkers, M.J., Klimowski, B.J., Zeitler, J.W., Thompson, R.L., Weisman, M.L., 2000. Predicting supercell motion using a new hodograph technique. Wea. Forecasting. 15, 61–79.

Childs, S.J., Schumacher, R.S., Allen, J.T., 2018. Cold-season tornadoes: climatological and meteorological insights. Wea. Forecasting. 33, 671–691. https://doi.org/10.1175/WAF-D-17-0120.1.

Craven, J.P., Brooks, H.E., 2004. Baseline climatology of sounding derived parameters associated with deep moist convection. Nat. Weath. Dig. 28, 13–24.

Davies, J.M., 2006. RUC soundings with cool season tornadoes in "small" CAPE settings and the 6 November 2005 Evansville, Indiana tornado. In: 23rd Conf. On Severe Local Storms. 4. Amer. Meteor. Soc., St. Louis, MO, pp. 3. https://ams.confex.com/ams/pdfpapers/115477.pdf.

Davies-Jones, R.P., 1986. Tornado dynamics. In: Kessler, E. (Ed.), Thunderstorm Morphology and Dynamics. University of Oklahoma Press, Norman, pp. 197–236.

Davies-Jones, R.P., 2008. An efficient and accurate method for computing the wet-bulb temperature along pseudoadiabats. Mon. Weather Rev. 136, 2764–2785. https://doi.org/10.1175/2007MWR2224.1.

Doswell III, C.A., 1998. Seeing supercells as heavy rain producers. In: Preprints, 14th Conf. On Hydrology. Amer. Meteor. Soc., Dallas, TX, pp. 73–79.

Doswell III, C.A., Brooks, H.E., Maddox, R.A., 1996. Flash-flood forecasting: an ingredients-based methodology. Weather Forecast. 11, 360–381.

Gensini, V.A., Marinaro, A., 2016. Tornado frequency in the United States related to global relative angular momentum. Mon. Weather Rev. 144, 801–810.

Gensini, V.G., Gold, D., Allen, J.T., Barrett, B.S., 2019. Extended U.S. tornado outbreak during late May 2019: a forecast of opportunity. Geophys. Res. Lett. 46, 10150–10158.

Grazzini, F., Vitart, F., 2015. Atmospheric predictability and rossby wave packets: Predictability and Rossby wave packets. Quart. J. Roy. Meteor. Soc. 141, 2793–2802. https://doi.org/10.1002/qj.2564.

Grimm, A.M., 2019. Madden–Julian Oscillation impacts on south American summer monsoon season: precipitation anomalies, extreme events, teleconnections, and role in the MJO cycle. Clim. Dyn. 53. https://doi.org/10.1007/s00382-019-04622-6.

Guyer, J.L., Imy, D.A., Kis, A.K., 2006. Cool season significant (F2–F5) tornadoes in the Gulf Coast states. In: 23rd Conf. On Severe Local Storms. 4. Amer. Meteor. Soc., St. Louis, MO, pp. 2. https://ams.confex.com/ams/23SLS/techprogram/paper_115320.htm.

Hales, J.E., 1985. Synoptic features associated with Los Angeles tornado occurrences. Bull. Amer. Meteor. Soc. 66, 657–662. https://doi.org/10.1175/1520-0477-66.6.657.

Hanstrum, B.N., Mills, G.A., Watson, A., 1998. Australian cool season tornadoes. Part 1: Synoptic climatology. In: Preprints, 19th Conf. On Severe Local Storms. Amer. Meteor. Soc., Minneapolis, MN, pp. 97–100.

Hanstrum, B.N., Mills, G.A., Watson, A., Monteverdi, J.P., Doswell, C.A., 2002. The cool-season tornadoes of California and southern Australia. Wea. Forecasting. 17, 705–722. https://doi.org/10.1175/1520-0434(2002)017<0705:TCSTOC>2.0.CO;2.

Iacono, M.J., Delamere, J.S., Mlawer, E.J., Shephard, M.W., Clough, S.A., Collins, W.D., 2008. Radiative forcing by long–lived greenhouse gases: Calculations with the AER radiative transfer models. J. Geophys. Res. 113, D13103. https://doi.org/10.1029/2008JD009944.

Jacques-Coper, M., Brönnimann, S., Martius, O., Vera, C.S., Cerne, S.B., 2015. Evidence for a modulation of the intraseasonal summer temperature in eastern Patagonia by the Madden-Julian Oscillation. J. Geophys. Res. Atmos. 120, 7340–7357. https://doi.org/10.1002/2014JD022924.

Janjic, Z.I., 1994. The step–mountain eta coordinate model: further developments of the convection, viscous sublayer, and turbulence closure schemes. Mon. Weather Rev. 122, 927–945.

Johnson, R.H., 2001. Surface mesohighs and mesolows. Bull. Amer. Meteor. Soc. 82, 13–32. https://doi.org/10.1175/1520-0477(2001)082<0013:SMAM>2.3.CO;2.

Juliá, C., Rahn, D.A., Rutllant, J.A., 2012. Assessing the influence of the MJO on strong precipitation events in subtropical, semi-arid north-Central Chile (30°S). J. Clim. 25, 7003–7013. https://doi.org/10.1175/JCLI-D-11-00679.1.

Kalnay, et al., 1996. The NCEP/NCAR 40-year reanalysis project. Bull. Amer. Meteor. Soc. 77, 437–470.

King, J.R., Parker, M.D., Sherburn, K.D., Lackmann, G.M., 2017. Rapid evolution of cool season, low-CAPE severe thunderstorm environments. Wea. Forecasting. 32, 763–779. https://doi.org/10.1175/WAF-D-16-0141.1.

Lackmann, G.M., Overland, J.E., 1989. Atmospheric structure and momentum balance during a gap-wind event in Shelikof Strait, Alaska. Mon. Weather Rev. 117, 1817–1833.

LaFleur, D.M., Barrett, B.S., Henderson, G.R., 2015. Some climatological aspects of the Madden-Julian Oscillation (MJO). J. Clim. 28, 6039–6053. https://doi.org/10.1175/JCLI-D-14-00744.1.

LaPenta, K.D., Bosart, L.F., Galarneau, T.J., Dickinson, M.J., 2005. A multiscale examination of the 31 May 1998 Mechanicsville, New York, tornado. Wea. Forecasting. 20, 494–516.

Lawrence, M.G., 2005. The relationship between relative humidity and the dewpoint temperature in moist air: a simple conversion and applications. Bull. Amer. Meteor. Soc. 86, 225–233. https://doi.org/10.1175/BAMS-86-2-225.

Lim, Y., Son, S., Kim, D., 2018. MJO Prediction Skill of the Subseasonal-to-Seasonal Prediction Models. J. Climate 31, 4075–4094. https://doi.org/10.1175/JCLI-D-17-0545.1.

Madden, R.A., Julian, P.R., 1972. Description of global-scale circulation cells in the tropics with a 40–50 day period. J. Atmos. Sci. 29, 1109–1123.

Marin, J.C., Barrett, B.S., 2017. Seasonal and intraseasonal variability of precipitable water vapor in the Chajnantor plateau. Chile. Int. J. Climatol. 37, 958–971. https://doi.org/10.1002/joc.5049.

Marwitz, J.D., 1987. Deep orographic storms over the Sierra Nevada. Part I: Thermodynamic and kinematic structure. J. Atmos. Sci. 44, 159–173.

Mercer, A.E., Shafer, C.M., Doswell, C.A., Leslie, L.M., Richman, M.B., 2009. Objective classification of tornadic and nontornadic severe weather outbreaks. Mon. Weather Rev. 137, 4355–4368. https://doi.org/10.1175/2009MWR2897.1.

Moller, A.R., Doswell III, C.A., Przybylinski, R., 1990. High-precipitation supercells: A conceptual model and documentation. In: Preprints, 16th Conf. On Severe Local Storms. Amer. Meteor. Soc., Kananskis Park, AB, Canada, pp. 52–57.

Monteverdi, J.P., Quadros, J., 1994. Convective and rotational parameters associated with three tornado episodes in northern and Central California. Wea. Forecasting. 9, 285–300.

Monteverdi, J.P., Doswell, C.A., Lipari, G.S., 2003. Shear parameter thresholds for forecasting tornadic thunderstorms in northern and Central California. Wea. Forecasting. 18, 357–370. https://doi.org/10.1175/1520-0434(2003)018<0357:SPTFFT>2.0.CO;2.

Mulder, K.J., Schultz, D.M., 2015. Climatology, storm morphologies, and environments of tornadoes in the British Isles: 1980–2012. Mon. Weather Rev. 143, 2224–2240. https://doi.org/10.1175/MWR-D-14-00299.1.

Nakanishi, M., Niino, H., 2006. An improved Mellor–Yamada level 3 model: its numerical stability and application to a regional prediction of advecting fog. Bound.-Layer Meteorol. 119, 397–407. https://doi.org/10.1007/s10546-005-9030-8.

Niu, G.-Y., Yang, Z.-L., Mitchell, K.E., Chen, F., Ek, M.B., Barlage, M., Kumar, A., Manning, K., Niyogi, D., Rosero, E., Tewari, M., Xia, Y., 2011. The community Noah land surface model with multiparameterization options (Noah–MP): 1. Model description and evaluation with local–scale measurements. J. Geophys. Res. 116,

D12109. https://doi.org/10.1029/2010JD015139.
Overland, J.E., 1984. Scale analysis of marine winds in straits and along mountainous coasts. Mon. Weather Rev. 112, 2530–2534.
Overland, J.E., Bond, N.A., 1993. The influence of coastal orography: the Yakutat storm. Mon. Weather Rev. 121, 1388–1397.
Parish, T.R., 1982. Barrier winds along the Sierra Nevada mountains. J. Appl. Meteorol. 21, 925–930.
Parker, S.S., 2010. Classic and HP Mini-Supercells in Southeast Oregon and Southwest Idaho on 3 May 2009. Preprints, 25th Conf. On Severe Local Storms. P8, Denver, CO, pp. 14.
Potvin, C.K., Elmore, K.L., Weiss, S.J., 2010. Assessing the impacts of proximity sounding criteria on the climatology of significant tornado environments. Wea. Forecasting. 25, 921–930. https://doi.org/10.1175/2010WAF2222368.1.
Ragsdale, K.M., Barrett, B.S., Testino, A.P., 2013. Variability of particulate matter (PM10) in Santiago, Chile by phase of the Madden-Julian Oscillation (MJO). Atmos. Environ. 81, 304–310.
Rasmussen, E.N., 2003. Refined supercell and tornado forecast parameters. Wea. Forecasting. 18, 530–535. https://doi.org/10.1175/1520-0434(2003)18<530:RSATFP>2.0.CO;2.
Rasmussen, E.N., Blanchard, D.O., 1998. A baseline climatology of sounding-derived supercell and tornado forecast parameters. Wea. Forecast. 13, 1148–1164.
Reynolds, R.W., Smith, T.M., Liu, C., Chelton, D.B., Casey, K.S., Schlax, M.G., 2007. Daily high-resolution-blended analyses for sea surface temperature. J. Clim. 20, 5473–5496. https://doi.org/10.1175/2007JCLI1824.1.
Romero, R., Gay, M., Doswell III, C.A., 2007. European climatology of severe convective storm environmental parameters: a test for significant tornado events. Atmos. Res. 83, 389–404. https://doi.org/10.1016/j.atmosres.2005.06.011.
Rondanelli, R., Hatchett, B., Rutllant, J.A., Bozkurt, D., Garreaud, R., 2019. Strongest MJO on Record Triggers Extreme Atacama Rainfall and Warmth in Antarctica. Geophys. Res. Lett. 46, 3482–3491.
Saha, S., et al., 2011. Updated daily. NCEP Climate Forecast System Version 2 (CFSv2) 6-hourly Products. In: Research Data Archive at the National Center for Atmospheric Research, Computational and Information Systems Laboratory, . https://doi.org/10.5065/D61C1TXF, Accessed date: 10 July 2019.
Schneider, R.S., Dean, A.R., 2008. A comprehensive 5-year severe storm environment climatology for the continental United States. In: Preprints, 24th Conf. on Severe Local Storms. Amer. Meteor. Soc., Savannah, GA [Available online athttps://ams.confex.com/ams/pdfpapers/141748.pdf.].
Schneider, R.S., Dean, A.R., Weiss, S.J., Bothwell, P.D., 2006. Analysis of estimated environments for 2004 and 2005 severe convective storm reports. In: Preprints, 23rd Conf. on Severe Local Storms. Amer. Meteor. Soc., St. Louis, MO 3.5. [Available online at https://ams.confex.com/ams/pdfpapers/115246.pdf.].
Schultz, C.J., Petersen, W.A., Carey, L.D., 2009. Preliminary development and evaluation of lightning jump algorithms for the real-time detection of severe weather. J. Appl. Meteorol. Climatol. 48, 2543–2563. https://doi.org/10.1175/2009JAMC2237.1.
Shafer, C.M., Mercer, A.E., Richman, M.B., Leslie, L.M., Doswell, C.A., 2012. An assessment of areal coverage of severe weather parameters for severe weather outbreak diagnosis. Wea. Forecasting. 27, 809–831. https://doi.org/10.1175/WAF-D-11-00142.1.
Sherburn, K.D., Parker, M.D., 2014. Climatology and ingredients of significant severe convection in high-shear, low-CAPE environments. Wea. Forecasting. 29, 854–877. https://doi.org/10.1175/WAF-D-13-00041.1.
Sherburn, K.D., Parker, M.D., King, J.R., Lackmann, G.M., 2016. Composite environments of severe and nonsevere high-shear, low-CAPE convective events. Wea. Forecasting. 31, 1899–1927. https://doi.org/10.1175/WAF-D-16-0086.1.
Sioutas, M.V., Keul, A.G., 2007. Waterspouts of the Adriatic, Ionian and Aegean Sea and their meteorological environment. Atmos. Res. 83, 542–557. https://doi.org/10.1016/j.atmosres.2005.08.009.
Skamarock, W.C., Coauthors, 2019. A Description of the Advanced Research WRF Model Version 4. NCAR Technical Note NCAR/TN-556+STR. pp. 145. https://doi.org/10.5065/1dfh-6p97.
Stough, S.M., Carey, L.D., Schultz, C.J., Bitzer, P.M., 2017. Investigating the relationship between lightning and mesocyclonic rotation in supercell thunderstorms. Wea. Forecasting. 32, 2237–2259. https://doi.org/10.1175/WAF-D-17-0025.1.
Thompson, G., Field, P.R., Rasmussen, R.M., Hall, W.D., 2008. Explicit forecasts of winter precipitation using an improved bulk microphysics scheme. Part II: implementation of a new snow parameterization. Mon. Weather Rev. 136, 5095–5115. https://doi.org/10.1175/2008MWR2387.1.
Thompson, D.B., Roundy, P.E., 2013. The relationship between the Madden-Julian Oscillation and US violent tornado outbreaks in the spring. Mon. Weather Rev. 141, 2087–2095. https://doi.org/10.1175/MWR-D-12-00173.1.
Tippett, M.K., 2018. Robustness of relations between the MJO and U.S. tornado occurrence. Mon. Weather Rev. 146, 3873–3884.
Trapp, R.J., Tessendorf, S.A., Godfrey, E.S., Brooks, H.E., 2005. Tornadoes from squall lines and bow echoes. Part I: Climatological distribution. Wea. Forecasting. 20, 23–34.
Turcotte, V., Vigneux, D., 1987. Severe thunderstorms and hail forecasting using derived parameters from standard RAOBS data. In: Preprints, Second Workshop on Operational meteorology. Atmos. Environ. Service/Canadian Meteorol. and Oceanogr., Halifax, Nova Scotia, Canada, pp. 142–153.
Viale, M., Norte, F.A., 2009. Strong cross-barrier flow under stable conditions producing intense winter orographic precipitation: a case study over the subtropical Central Andes. Wea. Forecasting. 24, 1009–1031. https://doi.org/10.1175/2009WAF2222168.1.
Viale, M., Nuñez, M.N., 2011. Climatology of winter orographic precipitation over the subtropical Central Andes and associated synoptic and regional characteristics. J. Hydrometeorol. 12, 481–507. https://doi.org/10.1175/2010JHM1284.1.
Vicencio, J., Reyes, A., Sánches, S., Padilla, R., Crespo, J., Campos, D., 2019. Informe especial: Tornados en la Región del Biobío. pp. 40. http://archivos.meteochile.gob.cl/portaldmc/meteochile/documentos/DMC-InfoEspecial_TornadosBiobio_v5black.pdf, Accessed date: 14 August 2019.
Weber, N.J., Mass, C.F., 2019. Subseasonal weather prediction in a global convection-permitting model. Bull. Am. Meteorol. Soc. 100, 1079–1089. https://doi.org/10.1175/BAMS-D-18-0210.1.
Weickmann, K., Berry, E., 2009. The tropical Madden-Julian Oscillation and the global wind oscillation. Mon. Weather Rev. 137, 1601–1614.
Weisman, M.L., Klemp, J.B., 1982. The dependence of numerically simulated convective storms on vertical wind shear and buoyancy. Mon. Weather Rev. 110, 504–520.
Wheeler, M.C., Hendon, H.H., 2004. An all-season real-time multivariate MJO index: Development of an index for monitoring and prediction. Mon. Weather Rev. 132, 1917–1932. https://doi.org/10.1175/1520-0493(2004)132%3C1917:AARMMI%3E2.0.CO;2.
Wrona, B., Avotniece, Z., 2015. The forecasting of tornado events: the synoptic background of two different tornado case studies. Meteorol. Hydrol. Water Manag. 51–58.
Yu, C.-K., Smull, B.F., 2000. Airborne Doppler observations of a landfalling cold front upstream of steep coastal orography. Mon. Weather Rev. 128, 1577–1603.